Real-time lift forecast of a NACA0012 airfoil maneuvering randomly under dynamic stall conditions at $Re \sim 10^5$

Donghyun Kim * and Themistoklis Sapsis †
Massachusetts Institute of Technology, Cambridge, MA, 02139

Dynamic stall is an abrupt flow separation phenomenon that occurs on airfoils rapidly changing their posture. Because it accompanies a rapid drop of lift, there have been attempts to prevent the dynamic stall by using techniques such as impulsive jets, plasma actuators, and morphing wings. To maximize their efficacy, this research aims for a real-time forecast of the lift coefficient of a NACA0012 airfoil pitching and plunging randomly under dynamic stall conditions at $Re \sim 10^5$ by using surface pressure sensors. A large eddy simulation is used to simulate the flow around a randomly maneuvering airfoil, and it is demonstrated that a fully connected neural network fed with discrete wavelet-transformed pressure signals is enough to predict the lift coefficient of the near future. Certain sensor locations are found to be more informative than others in such randomly fluctuating flow, unlike in quasi-periodic situations. A fast optimal sensor placement strategy is also proposed. It reveals that two pressure sensors near the leading edge, one on each side of the airfoil, can provide sufficient information for forecasting the lift of a randomly maneuvering airfoil.

I. Introduction

Dynamic stall is a common phenomenon in engineering applications, including helicopters [1, 2], wind turbines [3, 4], and micro aerial vehicles [5, 6]. It's a stall happening on airfoils rapidly changing its posture, characterized by delayed flow separation and overshoot and subsequent plummet of lift coefficient. Because an abrupt decrease in lift is undesirable in most applications, there have been continuous attempts to postpone or prevent dynamic stalls. Techniques used include impulsive jets [7], plasma actuators [4], and morphing wings [6]. In this research, we seek to predict dynamic stalls before they happen to maximize the efficacy of the various dynamic stall suppression schemes.

Due to its rich dynamics, there has been extensive research on the physics of the dynamic stall phenomenon from both experimental [8, 9] and numerical perspectives [10–12]. To name a few that are closely related to our research, Martinat et al. [13] have shown by simulations that the flow around a pitching airfoil at $Re \sim 10^5 - 10^6$ is practically two-dimensional during the upward pitching while the flow is strongly three-dimensional during the downward pitching. Sheng et al. [14] have proposed a non-dimensional reduced pitch rate concept that delimits the quasi-steady and dynamic

*Graduate student, Dept. Mechanical Engineering, molamola@mit.edu
†Professor, Dept. Mechanical Engineering, sapsis@mit.edu

stall. Gupta and Ansell [15, 16] have experimentally demonstrated that the dynamic stall is inherently a multiscale phenomenon. They have pointed out the Kelvin-Helmholtz instability to be the driving mechanism of the dynamic stall onset. Mayer et al. [17] and Raus et al. [18] have found that low-frequency components of the airfoil surface pressure and noise are amplified during the dynamic stall, from experiments conducted inside aeroacoustic wind tunnels.

Meanwhile, there also have been efforts to forecast system responses under dynamic stall and unsteady flow events in general. Dawson et al. [19] have used dynamic mode decomposition (DMD) to identify a piecewise-linear system equation that can be used to predict lift and drag response to the pitching motion of an airfoil in a slow stream of air. For the same purpose, Hemati et al. [20] have developed a quasi-linear parameter-varying model. Troshin and Seifert [21] have tried to predict the evolution of the proper orthogonal decomposition modes of the flow field around an airfoil maneuvering in a water tank, by using the airfoil posture information, forces on the airfoil, and time-delay neural network. Shi et al. [22] have applied DMD with time-delay embedding to relate the current pressure on a periodically pitching airfoil surface to the surface pressure of the near future. Siddiqui et al. [23] and Damiola et al. [24] have developed nonlinear state-space models that take the angle of attack as input and the lift as output. Rudy and Sapsis [25] have applied a long short-term memory neural network to predict intermittent but quasi-periodic fluctuations on stationary airfoils using surface pressure signals. Under the same configuration, Barthel and Sapsis [26] have found that even a very simple fully connected neural network can map amplitudes of characteristic frequency components to the drag coefficient of the near future.

The present study aims for real-time forecasting of lift coefficients by utilizing pressure probes placed on the randomly maneuvering airfoil surface. The random maneuver imposes additional complexity compared with previous work that has focused on quasi-periodic conditions [26]. Section II describes the computational fluid dynamics (CFD) method used to simulate the flow around the maneuvering airfoil. The lift coefficient forecasting algorithm and its results are presented in Sec. III. A fast optimal sensor placement strategy based on the covariance coefficient is proposed and is compared to the result of the R^2-based greedy sequential sensor selection. The present work is wrapped up with concluding remarks in Sec. V.

II. Numerical simulation

An open-source CFD software OpenFOAM® v2306 is used to simulate the flow around a maneuvering NACA0012 airfoil. We employ a large eddy simulation (LES) turbulence model to capture the three-dimensional flow's temporal dynamics within a reasonable computational cost. The computational domain is depicted in Fig. 1 (a). The domain height is $8c$ and the length is $12c$, where c is the chord length. A freestream boundary condition is imposed on the inlet, outlet, and top and bottom faces to minimize the domain size's effect on the flow around the airfoil. The domain width in the spanwise direction is $0.2c$ which is deemed enough to reproduce the real flow [27]. Periodic boundary condition is imposed on the front and back of the domain. A C-type overset mesh surrounds the airfoil so that the

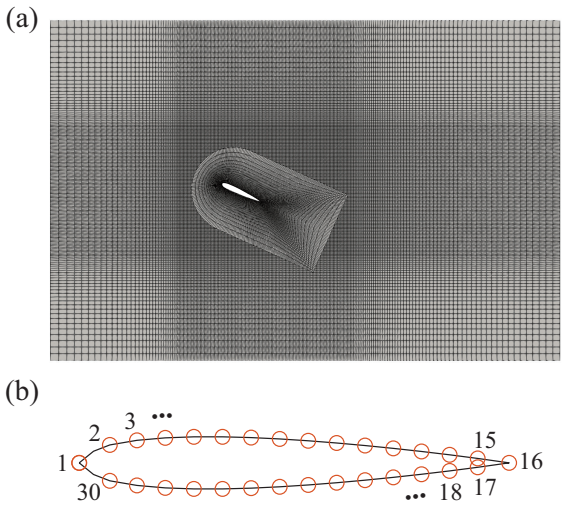

Fig. 1 (a) Computational domain of the LES simulation and (b) the locations of the pressure sensors.

maneuvering motion of the airfoil can be introduced. A compressible flow solver overRhoDyMPimpleFOAM solves the governing mass, momentum, and energy equations while ideal air is assumed. The subgrid-scale turbulence is modeled by a wall adapting local eddy viscosity (WALE) method [28], and the LES filter width is determined by a cube-root volume method. The eddy viscosity near the airfoil surface is calculated based on Spalding's near-wall velocity profile. Thirty pressure probes are uniformly placed along the airfoil mid-span profile to collect static pressure data from the simulation with 20 kHz frequency. The locations and numbering of the sensors are depicted in Fig. 1 (b). All of the simulations were done on MIT Supercloud TX-E1 [29] operated by the Lincoln Laboratory Supercomputing Center.

The numerical scheme is validated by comparison with the experimental measurement of a periodically pitching NACA0012 airfoil's lift coefficient done by Lee and Gerontakos [8] at $Re \sim 1.35 \cdot 10^5$. Although we are interested in a randomly maneuvering airfoil, the periodically pitching airfoil suffices for validation of the numerical simulation because essential flow features of dynamic stall are also present in it. The lift coefficient results from the experiment and numerical simulation are depicted in Fig. 2 to the changing angle of attack. The chord length $c = 0.15$ m, the freestream velocity $U_\infty = 14.0$ m/s, and the angle of attack $\alpha = \alpha_0 + \alpha_1 \sin(\omega t) = 10^\circ + 15^\circ \sin(18.7t)$. The center of rotation is located at $c/4$ from the leading edge. The simulation is conducted on three domains with different mesh sizes for a mesh dependence study. The specifications, namely the number of cells, the size of the cells right on the airfoil surface, and the required computational time are listed in Table 1. The Courant number is set to 0.3. The simulations are run for six pitching cycles (~ 2 s) and the time-synchronous averages are shown in the figure. The simulations took about 20 hours on mesh A, 60 hours on mesh B, and 100 hours on mesh C. Because the dynamic stall is a multiscale phenomenon as shown by Gupta and Ansell [16] driven by the small vortices inside shear layer, a more refined mesh and elaborate subgrid eddy viscosity model are desired for better accuracy of the LES simulation. However, the computational cost quickly reaches that of a direct numerical simulation as the mesh size decreases. Moreover, mesh B could at least capture

Name	Number of cells	Δx^+, Δz^+	Δy^+	Compute time (hr/s)
Mesh A	$1.2 \cdot 10^5$	< 180	< 30	10 (on 96 cores)
Mesh B	$4.1 \cdot 10^5$	< 120	< 20	30 (on 96 cores)
Mesh C	$9.6 \cdot 10^5$	< 90	< 15	50 (on 192 cores)

Table 1 Mesh specifications for mesh dependence study.

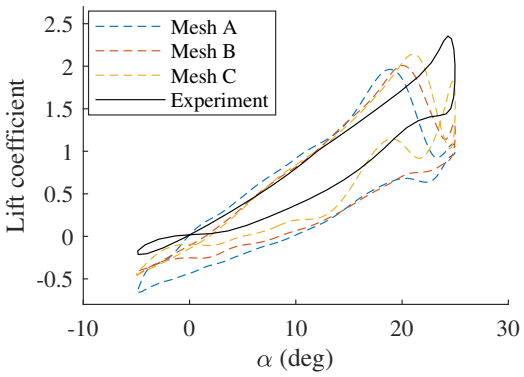

Fig. 2 Simulated and experimental lift coefficient history of a periodically pitching NACA0012 airfoil.

the two essential behaviors of the dynamic stall phenomenon: delayed stall and hysteresis. The stall is known to occur at an angle of attack between 10° and 12° when the NACA0012 airfoil is stationary, but the stall occurs at a higher angle of attack when the airfoil is pitching upward. Once the stall occurs, the flow remains separated during the downward pitching even at a much lower angle of attack, resulting in the lift coefficient hysteresis. Because a large amount of CFD data is required to train the lift coefficient prediction algorithm, we will use mesh B to compromise accuracy and computational cost. Also, we want to mention that a larger spanwise domain size of $0.5c$ gives the same result.

Illustrated in Fig. 3 are the snapshots of streamlines during the upward pitching and onset of the dynamic stall. The streamlines are colored based on the static pressure. The streamlines appear to be crossing each other in some pictures just because the flow is three-dimensional while we can only take two-dimensional snapshots. From Fig. 3, the flow is mostly attached to the airfoil surface when the angle of attack is small ($\alpha = 10.6°$). The vortex structure begins to appear at the leading edge as the angle of attack increases ($\alpha = 16.0°$). Here, a vortex structure is also observed on the trailing edge. The leading edge vortex structure enlarges as the angle of attack further increases, and eventually gets separated from the airfoil at an angle of attack between 20.6° and 22.4°. This large vortical structure is often called a dynamic stall vortex (DSV). The stall is continued at higher angles of attack ($\alpha = 24.6°$) and even during the downward pitching, resulting in the hysteresis of the lift coefficient shown in Fig. 2. For a more detailed description of the dynamic stall phenomena and its physics, see experimental studies by Gupta and Ansell [15, 16] and high-fidelity numerical studies by Martinat et al. [13] or Visbal and Garmann [11].

Figure 4 shows the continuous wavelet transform (CWT) result of the raw static pressure signal from probes 9 and

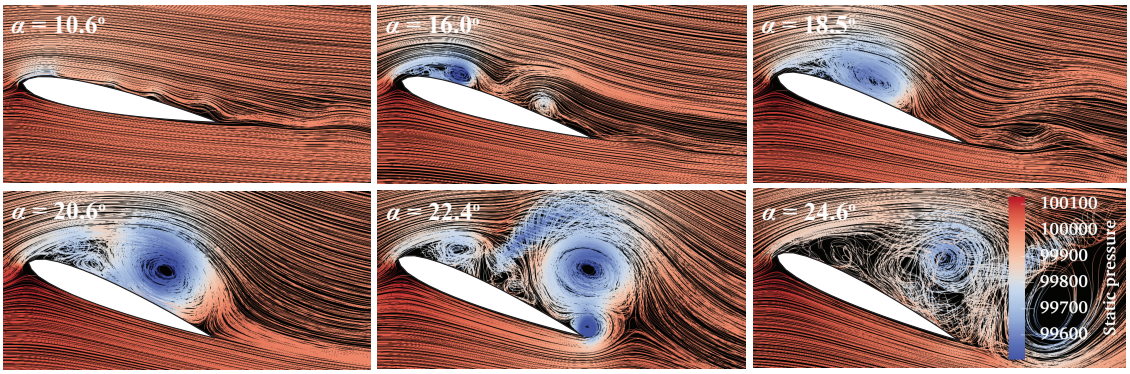

Fig. 3 Snapshots of streamlines around the pitching airfoil during the upward pitching and onset of the dynamic stall.

22 on the suction and pressure side of the airfoil, generated by using MATLAB®'s wavelet toolbox. The colors are in linear scale. A Morlet wavelet of symmetry parameter 3 and time-bandwidth product 60 was used. The two probes are in the middle of the airfoil's suction and pressure sides, symmetrical to the chord line. The lift coefficient history is placed on top of the CWT results for comparison. Peaks at low frequency $f = 10 - 40$ Hz are evident on the suction side when the airfoil begins to experience stall, while the pressure fluctuation is constantly small on the pressure side. The reduced frequency $k = \pi f c/U_\infty$ of the peak on the suction side is about one, corresponding to the time scale of large vortex structures such as the DSV. The burst of low-frequency pressure components on the airfoil surface at the onset of stall and flow reattachment of a dynamically pitching airfoil was also observed in recent experiments by Mayer et al. [17] and Raus et al. [18]. In our simulation, the peak is much stronger at the stall onset than at the flow reattachment because the pitching is fast enough that the stall phenomenon is dynamic rather than quasi-steady [14, 18].

III. Lift coefficient prediction under random maneuver

This work aims to forecast the lift coefficient of a randomly maneuvering NACA0012 airfoil. An Ornstein-Uhlenbeck (OU) process

$$\mathrm{d}X = (-X(t)/A + B^{1/2}\Gamma(t))\mathrm{d}t \tag{1}$$

and its exact numerical solution [30] is employed to model the random maneuvering motion of the airfoil. Here, A is the relaxation time, B is the diffusion coefficient, and $\Gamma(t)$ is a Gaussian white noise while the time step $\mathrm{d}t$ is 0.001 s. The original Matlab code for solving the stochastic differential equation is developed by Charlebois [31]. The resulting $X(t)$ is then multiplied by the amplitude of the pitching motion 15° or the amplitude of the plunging motion $c/2$. The OU process results are then smoothed to prevent the numerical divergence of the LES simulation. The relaxation time and

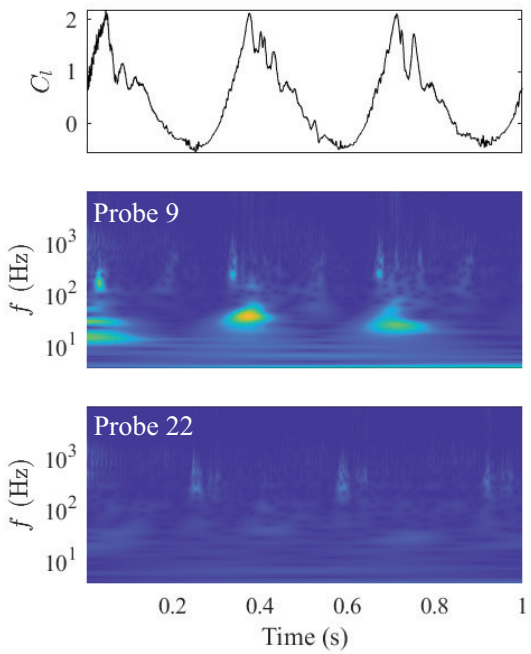

Fig. 4 Continuous wavelet transformed static pressure signals from probe 9 and probe 22 of the pitching airfoil.

diffusion coefficient of the process are carefully chosen to keep the speed of the pitching and plunging motion about and below the speed of the pitching motion tested in Sec. II. For instance, $A = 0.1$ s and $B = 10\ \mathrm{s}^{-2}$ for the pitching motion. An exemplary time history of the pitching angle and plunging displacement is depicted in Fig. 5. Here, Z_c is the z-direction displacement of the airfoil's center of rotation. The pitching and plunging motions are not strictly kept within the defined amplitude because the OU process is stochastic.

To forecast the lift coefficient of the airfoil, amplitudes of the dynamic stall's characteristic frequency ($f = 10 - 40$ Hz) are fed to a fully connected neural network (FCNN). The FCNN structure is simple:

$$\text{Input} \rightarrow \text{FC16} \rightarrow \tanh \rightarrow \text{FC16} \rightarrow \tanh \rightarrow \text{FC8} \rightarrow \text{FC4} \rightarrow \text{FC2} \rightarrow \text{FC1} \rightarrow \text{Output}. \tag{2}$$

The inputs to the neural network are $\gamma_n(t)$ and $\mathrm{d}\gamma_n(t)/\mathrm{d}t$, namely the amplitudes of the characteristic frequencies of the static pressure data acquired from the chosen probes, and their time derivatives. They characterize the onset of the dynamic stall, its current magnitude, and future trends. The output is the lift coefficient at $t + \Delta t$. Both $\gamma(t)$ and $C_l(t + \Delta t)$ are moving-averaged for smoothing by a window of size 5 samples to the past. Eight sets of five seconds of simulation are prepared to train and test the neural network. From the total 40 seconds of simulation, seven sets are used for training and the remaining 5 seconds of simulation are used to test the prediction algorithm. The first 0.2 s from each set are omitted from the data to remove the effect of initial condition and transiency which can also be seen in the first 0.1 s of Fig. 4.

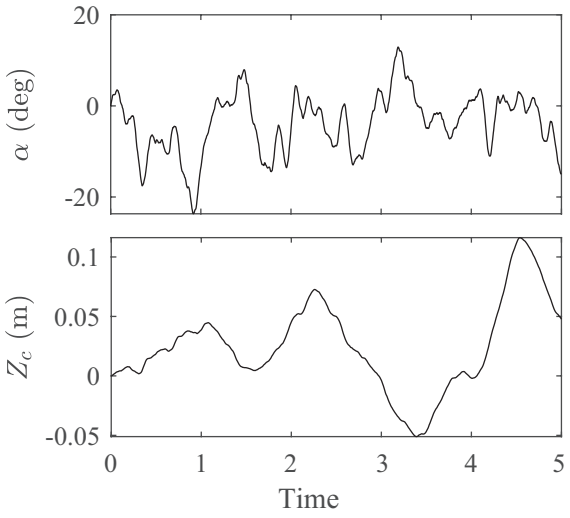

Fig. 5 An exemplary time history of the random pitching angle and plunging displacement.

While CWT is used in Barthel and Sapsis [26] to extract the characteristic frequency amplitudes, a discrete wavelet transform (DWT) was adopted in this study because DWT is much faster than CWT and thus is suitable for the real-time forecast of the lift coefficient. The DWT has also been applied for early warning of faults and failures in various systems, such as pipelines [32], aircraft spoilers [33], or axial compressors [34], due to its computational efficiency. The window size is set to 1024 sampling points to the past and DWT is done every 10 time steps. The sampling frequency is 20000 Hz, thus the window size is about 50 ms, and DWT is done every 0.5 ms. A Daubechies-2 wavelet and zero-padding are used. The amplitudes of the characteristic frequencies $\gamma_n(t)$ is $\gamma_{9,n}(t) + \gamma_{10,n}(t)/2$ where $\gamma_{9,n}(t)$ and $\gamma_{10,n}(t)$ are the 9^{th} and 10^{th} level DWT coefficients of the n^{th} pressure probe. Note that $\gamma_{9,n}(t)$ and $\gamma_{10,n}(t)$ corresponds to frequency components of $20-40$ Hz and $10-20$ Hz, respectively. Its time derivative is calculated by a first-order backward finite difference, $\mathrm{d}\gamma_n(t)/\mathrm{d}t \approx (\gamma_n(t) - \gamma_n(t-\delta t))/\delta t$ where δt is a single time step. The $\gamma_n(t)$ and $\mathrm{d}\gamma_n(t)/\mathrm{d}t$ are linearly normalized before being fed to the neural network such that their values lie between -1 and 1.

A modified version of output-weighted mean absolute error [35] is used as a loss function for training the neural network:

$$\mathrm{MAE}_{\mathrm{OW}}(\hat{C}_l; C_l) = \sum_{1}^{N} \frac{|\hat{C}_l - C_l|/N}{\max(\phi(\pm 1.5), \phi(\frac{C_l - \mu_{C_l}}{\sigma_{C_l}}))} \tag{3}$$

where N is the total number of training data, ϕ is the probability density of a normal distribution, and μ_{C_l} and σ_{C_l} are mean and standard deviation of the lift coefficient data for training. The output-weighted loss function is a special kind of loss function used to emphasize the rare events of large lift coefficients during the training process. The absolute error of the prediction is divided by the occurrence probability of the training data C_l so that the prediction becomes more accurate at high or low lift coefficients which correspond to dynamic stall. In this case, the weight is limited by $1/\phi(\pm 1.5) = 1/0.13 = 7.7$ which is manually tuned to prevent overfitting.

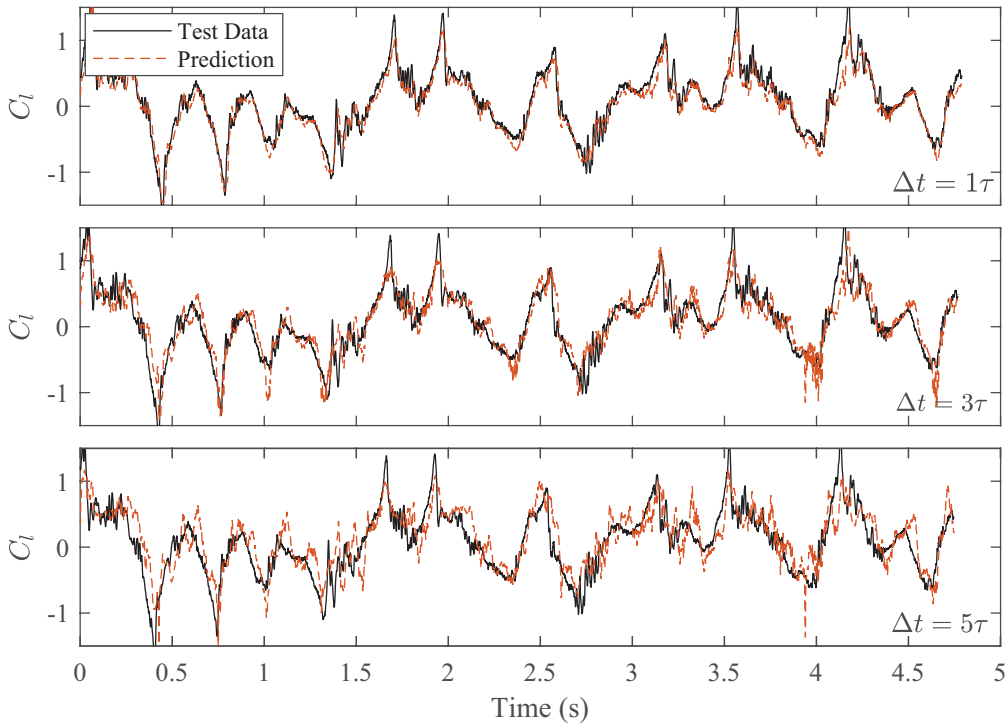

Fig. 6 The results of the lift coefficient prediction at $\Delta t = 1\tau$, $t = 3\tau$, and $\Delta t = 5\tau$

The results of the lift coefficient prediction at $\Delta t = 1\tau$, 3τ, and 5τ where $\tau = c/U_\infty$ are illustrated in Fig. 6. Pressure data from probes 4, 7, 28, and 29, which are found to be the optimal sensor locations in Sec. IV, are used. The DWT and neural network training are done on MATLAB®, using its wavelet and machine learning toolboxes. The predictions are satisfactory. The R^2 for different values of $\Delta t/\tau$ are summarized in Fig. 7. Here, $R^2 = \sqrt{\sum (\hat{C}_l - C_l/\bar{C}_l - C_l)^2}$ is a metric for goodness of fit which compares how the model better depicts the data than the mean value. The neural network is trained five times for each Δt and the mean and standard deviation of the R^2 values are calculated. The error bars in Fig. 7 correspond to ±3 standard deviations. At $\Delta t = 5\tau$, the R^2 is about 0.65. The forecasting performance decreases as Δt increases and the drop is larger at greater Δt. The horizon of the forecast seems to be related to the relaxation time $A = 0.1$ s $\sim 10\tau$ of the random maneuver. Beyond the relaxation time, the future airfoil motion is uncorrelated to the current airfoil motion thus the future lift is unpredictable. Also, note a slight difference in the wavelet transform schemes between this research and Barthel and Sapsis [26]: the entire signal was wavelet transformed together in the previous research such that future information is merged into the CWT results, especially at low frequencies. Frequency components of $fc/U_\infty \sim 0.4$, which corresponds to a period of $T \sim 2\tau$, was used in the previous research hence $\Delta t = 5\tau$ in this research is comparable to $\Delta t = 7\tau$ in Barthel and Sapsis [26].

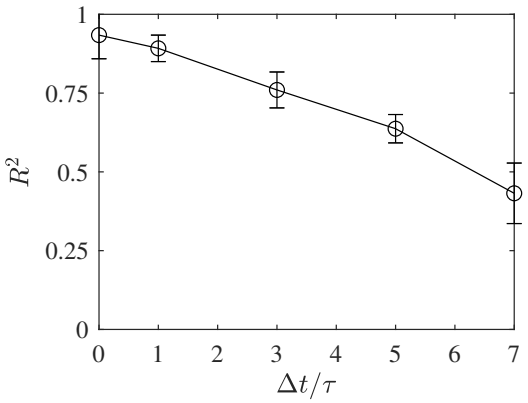

Fig. 7 The performance of the prediction algorithm for different values of Δt.

IV. Strategy for optimal sensor placement

The pressure probes must be optimally placed to use as few sensors as possible. Optimal sensor placement will reduce the computational cost of DWT, the complexity of the neural network, as well as the manufacturing cost. First, a greedy sequential sensor selection is conducted by using the R^2 of the trained neural networks to select the most efficient sensor locations. Given the neural network and a set of previously chosen n(S) pressure probes at the n(S) + 1^{th} sensor selection step, a new n(S) + 1^{th} pressure probe that best improves the R^2 is added to S. Here, S is the set of chosen sensors and n(S) is its number of elements. In every sensor selection step, for each candidate pressure probe, the FCNN has to be trained from its initial state to calculate R^2. This process is repeated, sequentially adding sensors to the airfoil surface until n(S) reaches the desired number of sensors. A pseudocode for the sequential sensor selection is introduced in Fig. 8 (a). To get the worst sensor choices, sensors that deteriorate R^2 the most are chosen in every sensor selection step. Note that Δt is fixed during the sensor selection process.

The best and worst choices, corresponding lift coefficient prediction results, and R^2 values to the increasing number of sensors are shown in Fig. 9. The targeting limit of forecast Δt is set to be 5τ. The error bars mean ± 1 standard deviation. In the best sensor configuration, the R^2 value improvement is marginal from the third sensor meaning that only two sensors are enough to predict the lift coefficient of a dynamically stalling airfoil. The first three probes, namely probes 29, 4, and 28, are located around the leading edge where DSV is generated and detached. The fourth sensor, probe 7 is relatively far from the leading edge but the effect of the fourth sensor is minimal. On the other hand, when sensors are placed near the trailing edge or at the very front of the leading edge where the flow is not so relevant to the generation and detachment of DSV, e.g. probes 2, 16, 18, and 15, the R^2 can reach negative values. Figure 9 (b) shows that the forecasting completely fails when the worst sensors are chosen.

Although this approach for optimal sensor placement is computationally less burdensome than the global search algorithm that has to test all cases, e.g. $\frac{30!}{26!4!} = 27405$ cases for four sensors, it is still a time-consuming job because the neural network has to be trained every sensor selection step for each $\mathrm{S} \cup \{m\}$. The computation is especially burdensome

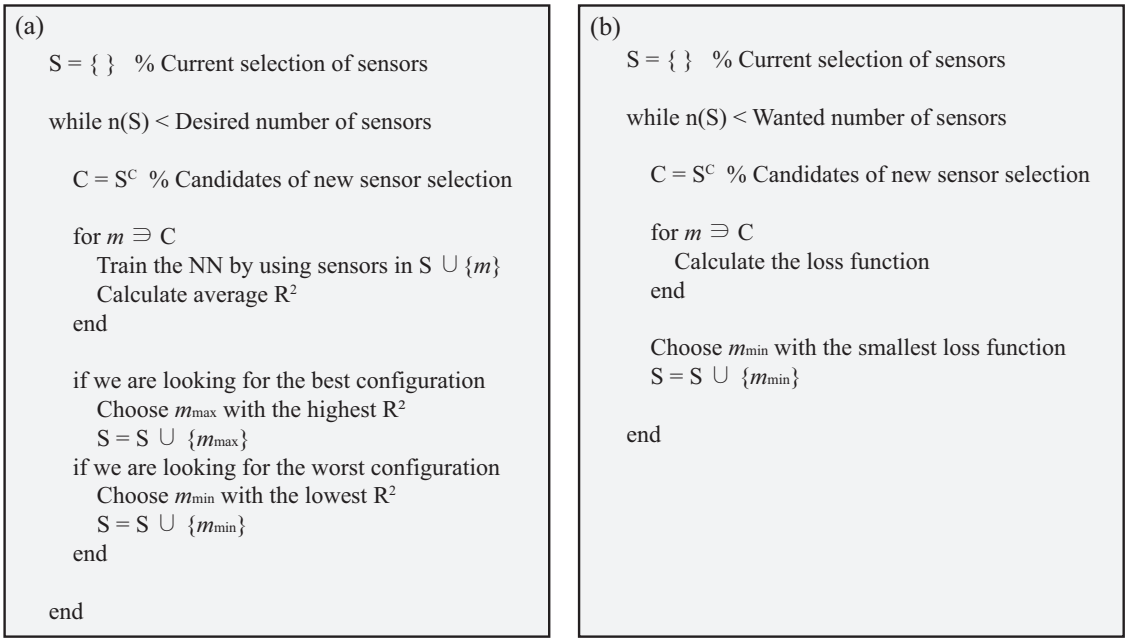

Fig. 8 Pseudocodes of the greedy sensor selection algorithms using (a) the R^2 of the trained neural networks (NN) and (b) the proposed loss function.

when we have a lot of training data and when we want an average of R^2. In our case, the neural network has been trained five times for each $\mathrm{S} \cup \{m\}$ to get the average R^2. Therefore, a fast offline strategy for optimal sensor selection is also desirable. In the context of greedy sequential sensor selection, the newly added pressure probe at every step must contain information relevant to the lift coefficient variation while containing new information as well. This means that the sensor selection is a dual-objective optimization problem: relevancy and novelty. To choose one sensor from the Pareto front composed of yet-to-selected sensors, a loss function that balances the two objectives should be devised:

$$-L(\gamma_n; C_{l,\Delta t}, \gamma_{m\in \mathrm{S}}) = \frac{|\rho(\gamma_n, C_{l,\Delta t})|}{\max_{n\in \mathrm{C}}(|\rho(\gamma_n, C_{l,\Delta t})|)} - \frac{\max_{m\in \mathrm{S}}(|\rho(\gamma_n, \gamma_m)|)}{\max_{n\in \mathrm{C}}(\max_{m\in \mathrm{S}}(|\rho(\gamma_n, \gamma_m)|))}. \tag{4}$$

Here, γ_n is the DWT coefficient of n^{th} sensor that is under consideration, $\gamma_{m\in \mathrm{S}}$ is the DWT coefficients of the already chosen n(S) sensors, C is the complement of S, and $\rho(\cdot, \cdot)$ is the correlation coefficient. The first term represents the relevance between the n^{th} probe's DWT data at t and the lift coefficient at $t + \Delta t$, while the second term stands for the relevance between the n^{th} probe and previously chosen n(S) sensors. The second term is subtracted to enhance the novelty of the newly added information. The denominators are included to normalize each term for fair balancing. Again note that Δt is fixed depending on the targeting limit of the forecast. The probe with the smallest loss function L is chosen in every sensor selection step. The pseudocode, which is similar to that of Fig. 8 (a) is introduced in Fig. 8 (b).

The chosen sensor locations are illustrated in Fig. 10 (a) together with the reference result of the R^2-based greedy approach. The targeting limit of forecasting Δt is set to be 5τ. The case in which only the first term of Eq. 4 is considered

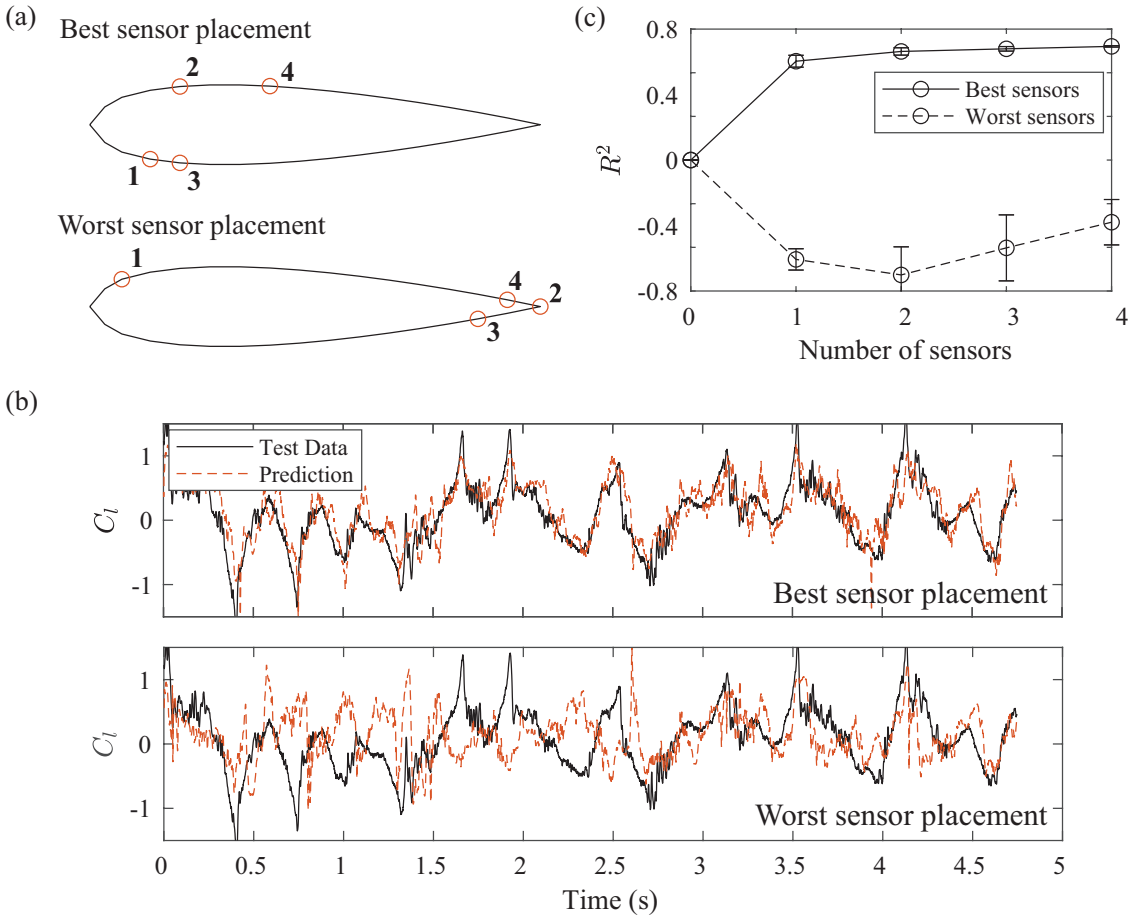

Fig. 9 (a) The best and worst sensor placements on the airfoil, (b) corresponding lift coefficient prediction results at $\Delta t = 5\tau$, and (c) R^2 values to increasing number of sensors at $\Delta t = 5\tau$.

for the loss function, i.e.

$$-l(\gamma_n; C_{l,\Delta t}) = \frac{|\rho(\gamma_n, C_{l,\Delta t})|}{\max_{n\in\mathbb{C}}(|\rho(\gamma_n, C_{l,\Delta t})|)} \tag{5}$$

is also shown for comparison. This means that the information from the newly added sensor doesn't have to be novel. The corresponding R^2 values are also illustrated in Fig. 10 (b). Again, the error bars mean ±1 standard deviation. When Eq. 4 is used for the loss function, the first three chosen probes are more or less the same as the reference, located around the leading edge of the airfoil. The difference is that the fourth sensor, probe 3, is also located around the leading edge, while the reference fourth sensor, probe 7, is located relatively away from the leading edge. But probe 3 is still not a bad choice; given the first three sensors (probes 4, 29, and 27), the R^2 after adding the fourth sensor can vary between 0.656 (probe 6) and 0.566 (probe 1) while probe 3 gives $R^2 = 0.647$. On the other hand, when Eq. 5 is used for the loss function, the first three sensors, probes 4, 3, and 5, are clustered on the upper side of the airfoil. The forecasting performance is not improved until a piece of new information is added by the fourth sensor, probe 27. We believe it's worth mentioning that the sensors are fairly placed on both sides of the airfoil for the best performance in our research because the angle of attack varies between ±15°. The pressure and suction sides interchange during the maneuvering, although not perfectly symmetric. If this is not the case, the best sensor placement could be inclined to the suction side of the airfoil where the important fluid dynamics appear.

The existence of optimal sensor locations differs from what was observed in quasi-periodic situations where no sensor location was superior to the others [26]. Figure 11 depicts the performance of the neural network trained and tested on a periodically pitching airfoil of Sec. II. 1.5 seconds of data are used for training and another 1.5 seconds for testing. The performance of the best sensors (4, 7, 28, 29) and the worst (2, 15, 16, 18), selected based on the randomly maneuvering airfoil data, are compared. The error bars represent the standard deviations. The R^2 values are more or less the same and this partially explains why fast sensor selection strategies didn't work successfully in Barthel and Sapsis [26]. Also, note that the R^2 values don't deteriorate significantly even if Δt increases when the flow is periodic.

V. Concluding remarks

This work aims to forecast the lift coefficient of an airfoil randomly maneuvering under dynamic stall conditions by using the surface pressure data, to maximize the efficacy of various dynamic stall suppression schemes. An FCNN coupled with DWT for forecasting the lift coefficient using the pressure data from probes on the airfoil surface is proposed. The data for training and testing the neural network is acquired from the LES simulation. It is demonstrated that low-frequency components corresponding to the large vortex structures are amplified during the onset of dynamic stall and that the DWT coefficients corresponding to these characteristic frequencies are good predictors of the lift coefficient. The forecast and the actual time series of the lift coefficient showed good agreement of R^2 about 0.65 at the forecasting limit of $\Delta t = 5\tau$.

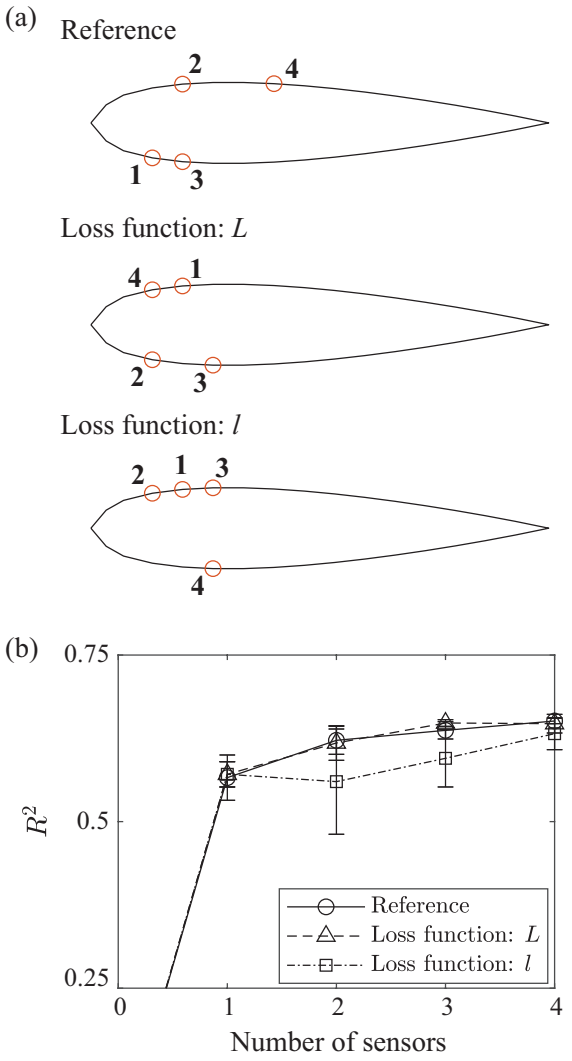

Fig. 10 (a) The chosen sensor locations and (b) corresponding R^2 to increasing number of sensors.

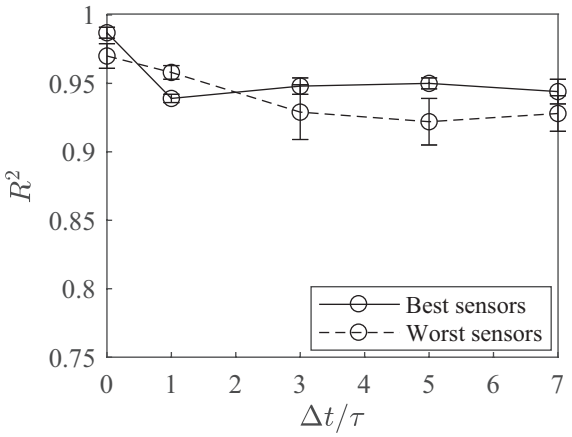

Fig. 11 Effect of the sensor locations in forecasting the lift of a periodically pitching airfoil.

Certain sensor locations are found to be more informative than others in such randomly fluctuating flow, unlike in quasi-periodic situations. A fast sequential sensor placement strategy is also proposed. The criterion of the sequential sensor selection is specially designed to balance the newly added data relevance to the future lift coefficient and novelty compared to the already chosen sensor data. The study shows that two pressure sensors located on the upper and lower sides of the airfoil, near the leading edge where important flow structures appear, are enough to predict the lift coefficient of the near future.

While the results are favorable, further experimental validation preferably at higher freestream velocity is necessary since our research is solely based on computational modeling. Randomly varying freestream velocity could also be incorporated in future research. Moreover, it is worth mentioning that the characteristic frequency utilized in this work is a consequence of the dynamic stall phenomenon rather than its driving mechanism. Though we could not capture the small turbulence structures due to our limited CFD fidelity, there certainly exists smaller vortex structures that precede the large vortex structures [16, 36]. We prospect to further increase the forecasting limit by utilizing the smaller turbulence structures that trigger the instability, which remains a topic of future research.

Funding Sources

We acknowledge support from the Army Research Office (Grant No. W911NF2010100), as well as the Air Force Office of Scientific Research (Grant No. FA9550-21-1-0058).

References

[1] Ham, N., and Garelick, M., "Dynamic stall considerations in helicopter rotors," *Journal of the American Helicopter Society*, Vol. 13(2), 1968, pp. 49–55.

[2] Mulleners, K., Kindler, K., and Raffel, M., "Dynamic stall on a fully equipped helicopter model," *Aerospace Science and Technology*, Vol. 19(1), 2012, pp. 72–76.

[3] Buchner, A., Soria, J., Honnery, D., and Smits, A., "Dynamic stall in vertical axis wind turbines: scaling and topological considerations," *Journal of Fluid Mechanics*, Vol. 841, 2018, pp. 746–766.

[4] Yu, H., Zhang, A., and Zheng, J., "Dynamic stall control for a vertical-axis wind turbine using plasma actuators," *AIAA Journal*, Vol. 61(11), 2023, pp. 4839–4851.

[5] Reich, G., Wojnar, M., and Albertani, R., "Aerodynamic performance of a notional perching MAV design," *47th AIAA Aerospace Science Meeting*, AIAA, 2009.

[6] Geissler, W., and van der Wall, B., "Dynamic stall control on flapping wing airfoils," *Aerospace Science and Technology*, Vol. 62, 2017, pp. 1–10.

[7] Kim, T., and Jee, S., "Numerical investigation of impulsively generated high-speed jet for dynamic stall suppression," *Computers & Fluids*, Vol. 251, 2023, p. 105757.

[8] Lee, T., and Gerontakos, P., "Investigation of flow over an oscillating airfoil," *Journal of Fluid Mechanics*, Vol. 512, 2004, pp. 313–341.

[9] Gao, Y., Zhu, Q., and Wang, L., "Measurement of unsteady transition on a pitching airfoil using dynamic pressure sensors," *Journal of Mechanical Science and Technology*, Vol. 30(10), 2016, pp. 4571–4578.

[10] Gharali, K., and Johnson, D., "Dynamic stall simulation of a pitching airfoil under unsteady freestream velocity," *Journal of Fluids and Structures*, Vol. 42, 2013, pp. 228–244.

[11] Visbal, M., and Garmann, D., "Analysis of dynamic stall on a pitching airfoil using high-fidelity large-eddy simulations," *AIAA Journal*, Vol. 56(1), 2018, pp. 46–63.

[12] Batther, J., and Lee, S., "Numerical investigation of a pitching airfoil undergoing dynamic stall using Delayed Detached Eddy Simulations," *Computers & Fluids*, Vol. 249, 2022, p. 105691.

[13] Martinat, G., Braza, M., Hoarau, Y., and Harran, G., "Turbulence modelling of the flow past a pitching NACA0012 airfoil at 10^5 and 10^6 Reynolds numbers," *Journal of Fluids and Structures*, Vol. 24, 2008, pp. 1294–1303.

[14] Sheng, W., Galbraith, R., and Coton, F., "Prediction of dynamic stall onset for oscillatory low-speed airfoils," *Journal of Fluids Engineering*, Vol. 130(10), 2008, p. 101204.

[15] Gupta, R., and Ansell, P., "Unsteady flow physics of airfoil dynamic stall," *AIAA Journal*, Vol. 57(1), 2019, pp. 165–175.

[16] Gupta, R., and Ansell, P., "Flow evolution and unsteady spectra of dynamic stall at transitional Reynolds numbers," *AIAA Journal*, Vol. 58(8), 2020, pp. 3272–3285.

[17] Mayer, Y., Zang, B., and Azarpeyvand, M., "A preliminary study of dynamic stall noise," *AIAA SciTech 2020 Forum*, AIAA, 2020.

[18] Raus, D., Cotté, B., Jondeau, E., Souchotte, P., and Roger, M., "Experimental study of the dynamic stall noise on an oscillating airfoil," *Journal of Sound and Vibration*, Vol. 537, 2022, p. 117144.

[19] Dawson, S., Schiavone, N., Rowley, C., and Williams, D., "A data-driven modeling framework for predicting forces and pressures on a rapidly pitching airfoil," *45th AIAA Fluid Dynamics Conference*, AIAA, 2015.

[20] Hemati, M., Dawson, S., and Rowley, C., "Parameter-varying aerodynamics models for aggressive pitching-response prediction," *AIAA Journal*, Vol. 55(3), 2017, pp. 693–701.

[21] Troshin, V., and Seifert, A., "Modeling of a pitching and plunging airfoil using experimental flow field and load measurements," *Experiments in Fluids*, Vol. 59, 2018, p. 6.

[22] Shi, Z., Zhou, K., Qin, C., and Wen, X., "Experimental study of dynamical airfoil and aerodynamic prediction," *Actuators*, Vol. 11(2), 2022, p. 46.

[23] Siddiqui, M., Troyer, T. D., Decuyper, J., Csurcsia, P., Schoukens, J., and Runacres, M., "A data-driven nonlinear state-space model of the unsteady lift force on a pitching wing," *Journal of Fluids and Structures*, Vol. 114, 2022, p. 103706.

[24] Damiola, L., Decuyper, J., Runacres, M., and Troyer, T. D., "Modeling airfoil dynamic stall using state-space Neural Networks," *AIAA SciTech 2023 Forum*, AIAA, 2023.

[25] Rudy, S., and Sapsis, T., "Prediction of intermittent fluctuations from surface pressure measurements on a turbulent airfoil," *AIAA Journal*, Vol. 60(7), 2022, pp. 4174–4190.

[26] Barthel, B., and Sapsis, T., "Harnessing instability mechanisms in airfoil flow for data-driven forecasting of extreme events," *AIAA Journal*, Vol. 61(11), 2023, pp. 4879–4896.

[27] Aihara, A., and Kawai, S., "Effects of spanwise domain size on LES-predicted aerodynamics of stalled airfoil," *AIAA Journal*, Vol. 61(3), 2023, pp. 1440–1446.

[28] Nicoud, F., and Ducros, F., "Subgrid-scale stress modeling based on the square of the velocity gradient tensor," *Flow, Turbulence and Combustion*, Vol. 62, 1999, pp. 183–200.

[29] Reuther, A., Kepner, J., Byun, C., Samsi, S., Arcand, W., Bestor, D., Bergeron, B., Gadepally, V., Houle, M., Hubbell, M., Jones, M., Klein, A., Milechin, L., Mullen, J., Prout, A., Rosa, A., Yee, C., and Michaleas, P., "Interactive supercomputing on 40,000 cores for machine learning and data analysis," *2018 IEEE High-Performance Extreme Computing Conference (HPEC)*, IEEE, 2018.

[30] Gillespie, D., "Exact numerical simulation of the Ornstein-Uhlenbeck process and its integral," *Physical Review E*, Vol. 54(2), 1996, pp. 2084–2091.

[31] Charlebois, D., "Exact numerical simulation of the Ornstein-Uhlenbeck process," , 2011. URL `https://www.mathworks.com/matlabcentral/fileexchange/30184-exact-numerical-simulation-of-the-ornstein-uhlenbeck-process`, accessed on Nov 01, 2023.

[32] Ferrante, M., Brunone, B., ASCE, M., and Meniconi, S., "Wavelets for the analysis of transient pressure signals for leak detection," *Journal of Hydraulic Engineering*, Vol. 133(11), 2007, pp. 1274–1282.

[33] Kordestani, M., Samadi, M., Saif, M., and Khorasani, K., "A new fault diagnosis of multifunctional spoiler system using integrated artificial neural network and discrete wavelet transform method," *IEEE Sensors Journal*, Vol. 18(12), 2018, pp. 4990–5001.

[34] Li, Y., Li, J., Du, J., Li, F., and Zhang, H., "Application of fast wavelet analysis on early stall warning in axial compressors," *Journal of Thermal Science*, Vol. 28, 2019, pp. 837–849.

[35] Rudy, S., and Sapsis, T., "Output-weighted and relative entropy loss functions for deep learning precursors of extreme events," *Physica D: Nonlinear Phenomena*, Vol. 443, 2023, p. 133570.

[36] Kern, J., Negi, P., Hanifi, A., and Henningson, D. S., "Onset of absolute instability on a pitching airfoi," , 2023. URL https://www.diva-portal.org/smash/get/diva2:1755843/FULLTEXT01.pdf, accessed on Jan 06, 2024.